Title

Osmium and lithium isotope evidence for weathering feedbacks linked to orbitally paced organic carbon burial and Silurian glaciations

Authors

Adam D. Sproson [a, b, *], Philip A. E. Pogge von Strandmann [c, d], David Selby [a, e], Emilia Jarochowska [f], Jiří Frýda [g, h], Jindřich Hladil [i], David K. Loydell [j], Ladislav Slavík [i], Mikael Calner [k], Georg Maier [f], Axel Munnecke [f], Timothy M. Lenton [l]

Affiliations

[a] Department of Earth Sciences, Durham University, Science Labs, Durham, DH1 3LE, UK.

[b] Biogeochemistry Research Center, Japan Agency for Marine-Earth Science and Technology, Yokosuka, Kanagawa 237-0061, Japan

[c] LOGIC, Institute of Earth and Planetary Sciences, University College London and Birkbeck, University of London, Gower Street, London, WC1E 6BT, UK.

[d] Institute of Geosciences, Johannes Gutenberg University, 55122 Mainz, Germany.

[e] State Key Laboratory of Geological Processes and Mineral Resources, School of Earth Resources, China University of Geosciences, Wuhan, 430074, Hubei, China.

[f] GeoZentrum Nordbayern, Friedrich-Alexander-Universität Erlangen-Nürnberg, Loewenichstraße 28, 91054 Erlangen, Germany

[g] Czech University of Life Sciences, Faculty of Environmental Sciences, Kamýcká 961/129, 165 21 Praha 6-Suchdol, Czech Republic.

[h] Czech Geological Survey, Klárov 3, 11821 Prague1, Czech Republic

[i] Institute of Geology of the Czech Academy of Sciences, Prague, Czech Republic

[j] School of the Environment, Geography and Geosciences, University of Portsmouth, Burnaby Road, Portsmouth PO1 3QL, UK.

[k] Department of Geology, Lund University, Sölvegatan 12, 223 62 Lund, Sweden.

[l] Global Systems Institute, University of Exeter, Laver Building (Level 8), North Park Road, Exeter, EX4 4QE, UK.

* corresponding author (adamsproson@gmail.com; sprosona@jamstec.go.jp)

Abstract

The Ordovician (~487 to 443 Ma) ended with the formation of extensive Southern Hemisphere ice sheets, known as the Hirnantian glaciation, and the second largest mass extinction in Earth History. It was followed by the Silurian (~443 to 419 Ma), one of the most climatically unstable periods of the Phanerozoic as evidenced by several large scale (> 5 ‰) carbon isotope ($\delta^{13}C$) perturbations associated with further extinction events. Despite several decades of research, the cause of these environmental instabilities remains enigmatic. Here, we provide osmium ($^{187}Os/^{188}Os$) and lithium ($\delta^{7}Li$) isotope measurements of marine sedimentary rocks that cover four Silurian $\delta^{13}C$ excursions. Osmium and Li isotope records resemble those previously recorded for the Hirnantian glaciation suggesting a similar causal mechanism. When combined with a new dynamic carbon-osmium-lithium biogeochemical model we suggest that astronomical forcing of the marine organic carbon cycle, as opposed to a decline in volcanic arc degassing or the rise of early land plants, resulted in drawdown of atmospheric CO_2, triggering continental scale glaciation, intense global cooling and eustatic sea-level lows recognised in the geological record. Lower atmospheric pCO_2 and temperatures during the Hirnantian and Silurian glaciations suppressed CO_2 removal by silicate weathering, driving $^{187}Os/^{188}Os$ and $\delta^{7}Li$ variability, supporting the existence of climate-regulating feedbacks.

Keywords: Osmium isotopes ($^{187}Os/^{188}Os$), Lithium isotopes ($\delta^{7}Li$), Silurian palaeoclimate, Hirnantian glaciation, Orbital obliquity, eccentricity and precession, Silicate weathering.

1. Introduction

The Earth's ecosystems underwent profound changes during the Ordovician and Silurian. Global cooling towards present-day equatorial sea surface temperatures (Trotter et al., 2008) coupled to a rise in atmospheric O_2 led to an abrupt increase in marine diversity during the Great Ordovician Biodiversification Event (Rasmussen et al., 2019). Increased volcanism during the Katian led to a gradual decline in biodiversity toward the end of the Ordovician, terminating with the Late Ordovician mass extinction (Rasmussen et al., 2019). This first of the Phanerozoic 'Big Five' extinctions coincided with the initiation of icehouse conditions and the extensive expansion of Southern Hemisphere continental ice, the Hirnantian glaciation (Algeo et al., 2016). A return to rapid biodiversity accumulation rates did not occur in the Silurian (Rasmussen et al., 2019), which was characterised by environmental instabilities linked to both minor and significant extinctions such as the 'Ireviken', 'Mulde', 'Lau' and 'Silurian-Devonian Boundary' bioevents (Fig. 1I; Calner, 2008).

The Hirnantian glaciation and Late Ordovician mass extinction are linked to a long-term decline in global temperatures brought about by some combination of: the enhanced weatherability of silicates, related to land-plant colonisation (Lenton et al., 2012) and/or the passage of fresh volcanic material through the tropics (Nardin et al., 2011); a reduction in volcanic arc degassing (McKenzie et al., 2016; Pogge von Strandmann et al., 2017); and/or an increase in organic carbon burial (Sproson, 2020). Although these processes continued to influence global climate well into the Silurian (Lenton et al., 2016; McKenzie et al., 2016; Nardin et al., 2011; Page et al., 2007), some explanations for Silurian bioevents have invoked a shift between two stable oceanic-climate states, driven by latitudinal changes in deep-water

formation (Jeppsson, 1990), or variations in global precipitation rates and continental runoff (Bickert et al., 1997). However, both the end-Ordovician and the Silurian extinction events are marked by similar variations in global $\delta^{13}C$ (Fig. 1J), oxygen isotopes ($\delta^{18}O$; Fig. 1L), eustatic sea-level (Fig. 1M) and lithological records (Calner, 2008; Munnecke et al., 2003), suggesting a similar causal link.

It has been postulated that Silurian climatic change and extinction events could have been driven by glacial expansion over Gondwana (Frýda et al., 2021; Munnecke et al., 2010; Trotter et al., 2016), much like the Late Ordovician that preceded it, astronomically paced by the ~4.5 Myr amplitude modulation of the cyclic eccentricity (400 kyr and 100 kyr) or obliquity (41 kyr) parameters of the Earth's axial motion and orbit (Sproson, 2020). Astronomical forcing of Silurian climate is supported by graptoloid turnover rates from the Late Ordovician to latest Silurian which correlate to the ~2.6 Myr eccentricity and ~1.3 Myr obliquity cycles (Crampton et al., 2018). Moreover, high resolution stratigraphic records for the Hirnantian glaciation suggest multiple glacial maxima paced by the ~1.2 Myr axial obliquity (Ghienne et al., 2014) or the ~100 kyr eccentricity (Sutcliffe et al., 2000) cycles. However, the lack of glacial sedimentary rocks in the post-Sheinwoodian stratigraphic record (Fig. 1K) has prevented the extension of astronomically paced glaciations as an explanation for Silurian climate events (Caputo et al., 1998; Díaz-Martínez and Grahn, 2007; Grahn and Caputo, 1992), despite indirect evidence of glaciation from dramatic facies changes in the Ludfordian which indicate a rapid worldwide shallowing (Frýda et al., 2021; Loydell and Frýda, 2011). Here, we provide Os and Li isotope records of sedimentary rocks – proxies for weathering processes and provenance – and a new dynamic carbon-osmium-lithium-model to test hypotheses for the cause(s) and nature of the Silurian events.

1.1 Tracing weathering using Os and Li isotopes

The Re-Os system undergoes parent-daughter fractionation during mantle melting leading to more radiogenic $^{187}Os/^{188}Os$ values in the upper continental crust relative to recent mantle derived minerals (Peucker-Ehrenbrink and Ravizza, 2000). The $^{187}Os/^{188}Os$ values of rivers are therefore seen to reflect the provenance of continental weathering, from the silicate weathering of unradiogenic juvenile basaltic minerals ($^{187}Os/^{188}Os$ = ~0.12) through to the oxidative weathering of highly radiogenic organic-sulphide-rich rocks ($^{187}Os/^{188}Os$ = ~1.37) (Georg et al., 2013). Stable Li isotopes, on the other hand, show limited fractionation during magmatic processes, and the primary components of the upper continental crust therefore display a narrow range of compositions (continental crust = ~0.6 ± 0.6 ‰, basalt = 0 to 5 ‰) (Sauzéat et al., 2015). However, Li isotopes fractionate significantly during chemical weathering, with the retention of ^{6}Li in weathering residues causing the $\delta^{7}Li$ values of rivers (2 to 44 ‰) to reflect 'weathering congruency', defined as the ratio of primary rock dissolution (congruent weathering drives rivers to low $\delta^{7}Li$), to secondary mineral (e.g., clays) formation (incongruent weathering drives rivers to high $\delta^{7}Li$) (Huh et al., 1998; Pogge von Strandmann et al., 2017).

The respective $^{187}Os/^{188}Os$ and $\delta^{7}Li$ of organic-rich shales and carbonates record the isotopic composition of seawater at the time of deposition (Peucker-Ehrenbrink and Ravizza, 2000; Pogge von Strandmann et al., 2017). In the modern oceans, the $^{187}Os/^{188}Os$ and $\delta^{7}Li$ of seawater ($^{187}Os/^{188}Os$ = ~1.06, $\delta^{7}Li$ = ~31 ‰) reflect the balance between riverine inputs ($^{187}Os/^{188}Os$ = ~1.54, $\delta^{7}Li$ = ~23 ‰), hydrothermal inputs ($^{187}Os/^{188}Os$ = ~0.12, $\delta^{7}Li$ = ~7 ‰), cosmogenic inputs ($^{187}Os/^{188}Os$ = ~0.13), and outputs related to the incorporation of Li into low-temperature marine clays, which impose a fractionation of ~15 ‰, and the scavenging of Os by organic or particulate matter (Misra and Froelich, 2012; Peucker-Ehrenbrink and Ravizza, 2000). The residence time of Os (~10-60 kyr) and Li (~1.2 Myr) in the ocean has allowed variations in these inputs and outputs, inferred from changes in the

125 sedimentary records of seawater $^{187}Os/^{188}Os$ and $\delta^{7}Li$, to provide unparalleled information
126 concerning the response of weathering to climatic and geological events (Misra and Froelich,
127 2012; Peucker-Ehrenbrink and Ravizza, 2000).
128
129 **2. Materials and methods**
130 **2.1 Palaeogeographic setting and sampling strategy**
131 To explore the response of weathering to climatic change during Silurian bioevents we
132 determined the respective $^{187}Os/^{188}Os$ and $\delta^{7}Li$ composition of three shale sections and three
133 carbonate sections that span much of the Silurian and include significant positive $\delta^{13}C$
134 excursions and extinctions: early Sheinwoodian (Aizpute-41 core, Latvia; Lusklint &
135 Lickershamn, Sweden); mid-Homerian (Bartoszyce core, Poland; Hunninge-1 core, Sweden);
136 and mid-Ludfordian (Kosov, Czech Republic), and the $^{187}Os/^{188}Os$ composition of a further
137 shale section (Klonk core, Czech Republic) that spans the Přídolí-Lochkovian boundary (see
138 *Supplementary Material*). Carbonate sections from Gotland (Sweden) and shale sections from
139 Latvia and Poland were respectively deposited in the shallow- and deep-waters of an
140 epicontinental sea to the north of the Rheic Ocean, whereas sections from the Czech Republic
141 represent deeper shelf sediments from the north coast of Gondwana, to the south of the Rheic
142 ocean (Fig. 1A).
143
144 **2.2 Sample preparation**
145 Prior to crushing, 20-80 g of shale samples were polished to eliminate contamination from
146 cutting and drilling marks and samples with any signs of veining or weathering were avoided.
147 The shale samples were then dried at 60 °C for ~12 h before being broken into chips with no
148 metal contact. Bulk carbonates and shales were crushed to a fine powder (~30 μm) in a
149 Zirconia ceramic dish using a shatterbox. Bulk carbonates were leached using a sequential

extraction method (Pogge von Strandmann et al., 2013), whereby ~0.1 g of carbonate was leached for 5 h at room temperature using Na acetate buffered to pH 5 by acetic acid. The sample preparation and Re-Os isotope and trace metal analysis were carried out at the Durham Geochemistry Centre (Laboratory for Sulfide and Source Rock Geochronology and Geochemistry) at Durham University. The Li isotope analysis was carried out at the stable isotope laboratory at the University of Oxford and later at the London Geochemistry and Isotope Centre at UCL.

2.3 Osmium isotope analysis of shales

Rhenium and Os abundances and isotopic compositions were determined using isotope dilution negative thermal ionisation mass spectrometry using Cr^{VI}–H_2SO_4 digestion and solvent extraction ($CHCl_3$), micro-distillation and anion chromatography methods (Creaser et al., 1991; Cumming et al., 2013; Selby and Creaser, 2003). The Cr^{VI}–H_2SO_4 digestion employed here principally dissolves the organic fraction of a shale, thus liberating the hydrogenous Re-Os load of the sediment and therefore avoiding detrital contamination (Selby and Creaser, 2003). The isolated Re and Os fractions were loaded onto Ni and Pt filaments respectively, and their isotopic composition was determined using a ThermoScientific TRITON mass spectrometer using Faraday collectors and the secondary electron multiplier, respectively.

Total procedural blanks for Re and Os are 10.09 ± 0.99 and 0.11 ± 0.06 pg respectively, with an average $^{187}Os/^{188}Os$ of 0.77 ± 0.54 (1SD; n=5). Raw Re and Os oxide values were corrected for oxygen contribution and mass fractionation. Calculated uncertainties include those associated with mass spectrometer measurements, blank abundance and isotopic composition, spike calibration, and sample and spike weights. In-house standard solutions of Re and Os (DROsS) yield an average $^{185}Re/^{187}Re$ value of

175 0.59872 ± 0.00135 (1SD, n = 24), and $^{187}Os/^{188}Os$ of 0.16101 ± 0.000401 (1SD, n = 41),
176 respectively, which is identical to previously published values (Nowell et al., 2008).
177 Initial $^{187}Os/^{188}Os$ ($^{187}Os/^{188}Os_i$) values in this study were determined from Re-Os data
178 and the ^{187}Re decay constant ($1.666e^{-11}$ a^{-1}) (Smoliar et al., 1996) and interpolated graptolite
179 biozone ages (Fig. S8). Analytical uncertainty for individual calculated Os_i is < 0.05. The
180 reproducibility of calculated $^{187}Os/^{188}Os_i$ was based on 15 analyses of the USGS rock
181 reference material SBC-1 (Bush Creek Shale) which has a value of ~0.65 ± 0.07 (2SD; Table
182 S4). Calculated $^{187}Os/^{188}Os_i$ ratios assume closed system behaviour after deposition and
183 therefore reflects the isotope composition of the local seawater at the time of sediment
184 deposition.
185
186 **2.4 Lithium isotope analysis of bulk carbonates**
187 A split of each sample solution was retained for cation analysis using an Elan Quadrupole
188 inductively coupled plasma mass spectrometer. Samples were matrix matched to 10 μg/g Ca
189 and calibrated against a set of synthetic standards made up from single element solutions. The
190 Al/Ca and Mn/Ca ratios were monitored to detect the influence of Li leached from clays.
191 Previous work suggests that carbonates must be >0.8 mmol/mol before carbonate Li isotope
192 ratios become measurably perturbed by Li leached from clays (Pogge von Strandmann et al.,
193 2013). Accuracy and precision were assessed by repeated analyses of seawater, JLs-1, and
194 repeated dissolutions of the Plenus Marl from Eastbourne. Sample reproducibility of Li/Ca
195 and Al/Ca was ~7% (2 SD, n=6). The larger part of each sample (typically containing 5-10
196 ng Li) was purified by passing it through a two-stage cation-exchange procedure (Pogge von
197 Strandmann et al., 2017; Pogge von Strandmann et al., 2019). Given that Li isotopes
198 fractionate during cation chromatography, it is critical to have column yields close to 100%.

To assess the efficacy of this process, splits of the solution were collected before and after the collected bracket for Li, which were shown to have <0.1% of Li.

The total procedural blank for Li isotope analysis is ~0.02 ng Li, which is insignificant compared to the mass of sample used. Analyses were performed on a Nu Plasma HR multi-collector ICP-MS at Oxford, and a Nu Plasma 3 MC-ICP-MS at UCL, using a sample-standard bracketing system relative to the LSVEC standard (Flesch et al., 1973). Each sample was measured three separate times during the same analytical session. Each individual measurement consisted of 10 ratios (10 s total integration time), giving a total integration time of 300 s/sample. At an uptake rate of 75 µl/min, the sensitivity for a 20 ng/ml solution is ~180 pA of ^{7}Li at Oxford (Pogge von Strandmann et al., 2019). Background instrumental Li intensity, typically ~0.01 pA, was subtracted from each measurement. Accuracy and external reproducibility, as assessed from seawater, is 31.1 ± 0.6 ‰ (2 SD, n = 16). Precision was also assessed from repeated analyses of an in-house marl standard, which also gives a reproducibility of ± 0.6 ‰ (n = 7). At UCL, a 5 ng/ml solution gives around 120 pA of ^{7}Li.

2.5 Dynamic C-Os-Li geochemical model

We developed a simple coupled carbon-cycle-climate model to explore potential drivers of new (^{187}Os/^{188}Os, δ^{7}Li) and existing (δ^{13}C, δ^{18}O) isotope data over relatively short-term events in the Silurian. The carbon cycle component of the model is based on the GEOCARBSULF (Berner, 2006) and COPSE (Lenton et al., 2018) biogeochemical models, and the simple model used by Pogge von Strandmann *et al.* (2017) to study the Hirnantian, adding osmium cycling (Lechler et al., 2015; Pogge von Strandmann et al., 2013) to the existing lithium cycle. In essence, the model interactively captures the long-term inorganic carbon cycle with degassing input of CO_2, and any imbalance in the organic carbon cycle

such as carbon burial, assumed to be balanced by CO_2 drawdown from silicate weathering. Silicate weathering depends on CO_2, temperature, and vegetation, providing negative feedback on climate variations. Silicate weathering, along with hydrothermal activity, drives input fluxes of Li and Os to the ocean and is balanced by sedimentary removal. A threshold response model is also considered to generate large (~5 ‰) $\delta^{13}C$ variations via the growth and decay of the marine organic carbon reservoir (Laurin et al., 2015), driven by numerical solutions for orbital precession and obliquity (Laskar et al., 2004). The climate component of the model – capturing changes in global temperature and ice sheet extent – is based on a logarithmic relationship between CO_2 and radiative forcing from the GCM-ice sheet modelling results of Pohl *et al.* (2016). The model is solved numerically using Euler's method run from initial values (Table S3) at a timestep of 5000 years. A detailed description of the model can be found in the *Supplementary Material*.

Key parameter settings for initialising the model are the rates of tectonic degassing and uplift, the areal coverage of land plants, and their effect on weathering. Normalised forcing factors for degassing (D), uplift (U), vegetation (V) and weathering (W) are derived from the COPSE and GEOCARBSULF biogeochemical model estimates for the Silurian (see Fig. 3 in Lenton et al. (2018)). Degassing was elevated relative to the present and we use an estimate for the start of the Silurian at ~443 Ma (D = 1.5). Uplift was comparable to today's conditions, and we use an average estimate for the Silurian (U = 0.94). The first non-vascular plants had colonised the land surface during the Late Ordovician, establishing an assumed modest fractional coverage (V = 0.15) but with a substantial effect on weathering (W = 0.75), consistent with previous work (Pogge von Strandmann et al., 2017). A key difference from GEOCARBSULF, which has been explored in COPSE (Lenton et al., 2018), is that we assume a larger plant amplification effect on weathering today (k_v^{-1}) of a factor of 10 rather than a factor of 4. To test different hypotheses, the model is either perturbed after 0.5 Myr by

changing forcing factors D, U, V or W, or subjected to orbital forcing from numerical solutions for precession or obliquity.

3. Results and discussion

3.1 Os and Li isotope records for the Silurian

New $^{187}Os/^{188}Os$ and $\delta^{7}Li$ profiles for these sections have been compiled with existing $\delta^{13}C$ and $\delta^{18}O$ profiles and show similar trends for each time period studied, but with differing magnitudes of change (Fig. 1B-1H and S1-S7; Table S1-S2). Prior to a $\delta^{13}C$ excursion there is a positive shift of magnitude 0.19 to 0.56 in the $^{187}Os/^{188}Os$ composition, often associated with a positive shift in $\delta^{18}O$ of magnitude 0.55 to 1.74 ‰. This is followed by a decline in the $^{187}Os/^{188}Os$ composition to pre-excursion values. During the $\delta^{13}C$ excursions, of magnitude 0.9 to 8.29 ‰, the $^{187}Os/^{188}Os$ composition generally remains low. In contrast, the $\delta^{7}Li$ of carbonates displays a positive shift of magnitude 4.7 to 9.6 ‰. During a plateau in $\delta^{13}C$ values, the $\delta^{18}O$ and $\delta^{7}Li$ values begin to return to pre-excursion values in some sections. During this decline, the $^{187}Os/^{188}Os$ values observe a second positive shift of magnitude 0.26 to 0.8 before returning to pre-excursion values either synchronously with the descending limb of the $\delta^{13}C$ record or prior to it.

Processes that could cause these variations include contamination during sample processing, diagenesis, or a primary seawater signal driven by changes in Earth system processes. Contamination of Re and Os from the detrital fraction of shales was avoided by using the CrO_3–H_2SO_4 digestion method, while cation exchange or leaching of clays, which could impart an isotopically light $\delta^{7}Li$ signal, was monitored by analysing cation/Ca ratios of carbonates. Diagenesis can be discounted because the shale sections studied here show no signs of veining or metamorphism suggesting that the extracted organic-phase-Os remains unaltered (Selby and Creaser, 2003) and cation/Ca ratios display no discernible trend with

δ^7Li (Table S2). Furthermore, δ^{13}C and δ^{18}O values in studied profiles (Fig. S1-S7) show similar values to other correlated sections that span the same intervals (Fig. 1J and 1L). It is therefore suggested that the isotopic shifts in the shale and carbonate sections represent primary seawater signatures.

When compiled onto our new age-depth model (Fig. S8), variations in $^{187}Os/^{188}Os$ and δ^7Li from this study (Fig. 2B-E) compare well, in terms of magnitude and timing of change, to records for the Hirnantian (Fig. 2A) suggesting similar causal processes. In general, we observe two peaks of radiogenic $^{187}Os/^{188}Os$ (centred around the vertical grey dashed line) separated by ~270-700 kyr (mean = 550 kyr; σ = 180) and an ascending limb of δ^7Li toward peak values (vertical black dashed line), which occurs ~210-630 kyr (mean = 450 kyr; σ = 180) after the first peak in radiogenic $^{187}Os/^{188}Os$ (Fig. 2). These broadly consistent patterns of change provide a target for numerical modelling. We use the model to test a series of hypotheses, attempting to reproduce: (1) the double-peaked $^{187}Os/^{188}Os$ response of magnitude 0.2 to 0.8; (2) a single transient peak of δ^7Li (>5 ‰); (3) $\delta^{13}C_{carb}$ variation of ~2-8 ‰ over ~1 to 2.5 Myr (Fig. 1J); (4) $\delta^{18}O_{phos}$ variation of ~1-2 ‰ over ~1 to 2 Myr (Fig. 1L); and, (5) sea-level drops of ~50-200 m over ~1 Myr (Fig. 1M).

3.2 Initial state of the C-Os-Li geochemical model

The relatively low plant cover of the Silurian, and corresponding suppression of the large assumed effect of plants on weathering, produces a high steady state CO_2 at ~16 PAL (and a global temperature relative to the present day, ΔT, of ~9K), which is consistent with the lack of a large, permanent ice sheet from the climate-ice sheet simulations of Pohl *et al.* (2016) for the Late Ordovician. A modest ice sheet extent of ~2 Mkm^2 is predicted and fixed at this value in the model variant without interactive ice sheets. The initial model state is poised to grow an ice sheet if that option is included and CO_2 declines, which is reasonable given that

299 the Hirnantian experienced a pronounced ice age. Initialising the model with higher D, lower
300 U, V, or W, would all tend to increase the initial CO_2 making it harder to trigger glaciation.
301 In the initial state the ocean Li reservoir is ~4 x 10^{16} mol, δ^7Li_{sw} = 17.5 ‰, and
302 δ^7Li_{carb} = 13.5 ‰, higher than the data, but close to the minimum allowable from isotopic
303 mass balance (Fig. 1F to H). The Os reservoir is ~1 x 10^8 mol with a $^{187}Os/^{188}Os$ of 0.64, in
304 the range of the data (Fig. 1B to E). An initial $\delta^{13}C$ of 1 ‰ is a reasonable baseline value for
305 the Silurian (Fig. 1J). We begin by testing the hypotheses previously proposed as drivers of
306 Hirnantian climate change, notably a decline in volcanic arc degassing and the colonisation
307 of land plants, before considering orbital forcing of imbalances in organic carbon burial and
308 the possibility of widespread Southern Hemisphere glaciations.
309
310 **3.3 Can tectonic or biological forcing explain observed Os and Li isotope records?**
311 Variations in the δ^7Li of seawater during the Hirnantian (Fig. 2A) have been linked to a
312 decrease in silicate weathering caused by a decline in global temperatures, ultimately linked
313 to a decline in CO_2 degassing. Continental arc volcanism continued to decline into the
314 Silurian (McKenzie et al., 2016) as the Iapetus Ocean closed during the formation of
315 Laurussia suggesting a possible link between degassing and our Os and Li isotope records.
316 An extreme halving of degassing over 1 Myr (Fig. 3A), which is unprecedented for the
317 Phanerozoic, causes a halving of atmospheric CO_2 and a global cooling of ~4 °C (Fig. 3B),
318 driving an increase in $\delta^{18}O_{phos}$ of 0.8 ‰ (Fig. 3C). A halving of the riverine and hydrothermal
319 fluxes coupled to a reduction in the oceanic Li reservoir drives a ~3 ‰ positive δ^7Li
320 excursion over ~3 Myr (Fig. 3C). Ocean Os content drops more rapidly, and because the
321 unradiogenic hydrothermal and basalt weathering input halves, whilst relatively radiogenic
322 sediment weathering remains constant, the $^{187}Os/^{188}Os$ of seawater increases by ~0.19 (Fig.
323 3C). Although O, Li and Os variation is in the same direction as Silurian records, the

variation is too small and not transient (Fig. 2 and 1L), displaying a permanent shift to higher values (Fig. 3C). This suggests that even an abrupt and rapid decline in degassing cannot (on its own) explain the Li and Os isotope variations during the Silurian (or Hirnantian) events and transient changes in degassing are assumed not to be applicable for the timescales under consideration.

The evolution of non-vascular land plants had a potentially profound effect on silicate weathering fluxes during the Late Ordovician (Lenton et al., 2012). In the Silurian, their spread was augmented by the evolution of the first vascular land plants (Lenton et al., 2016). Conceivably, expansions in plant cover and associated increases in global weathering rates occurred during the Silurian (Lenton et al., 2016), albeit of uncertain magnitude. Modelling an extreme doubling of vegetation cover over 1 Myr (Fig. 3D) causes CO_2 to decline by ~2.5 PAL, a < 2°C cooling (Fig. 3E) and a stepwise increase in $\delta^{18}O$ (Fig. 3F). The increase in silicate weathering, by ~10 % until CO_2 and temperature have adjusted, brought on by land plant proliferation drives a transient negative ~0.6 ‰ excursion in $\delta^{7}Li$ (Fig. 3F) because the unfractionated riverine source increases. The weathering of more radiogenic granitic and sedimentary rocks drives a similar transient decrease in the $^{187}Os/^{188}Os$ of ~0.02 (Fig. 3F). Neither isotopic response is in the direction observed in Silurian records (Fig. 2).

If we include an intensification of pedogenesis and clay formation via incongruent weathering, the riverine $\delta^{7}Li$, and therefore oceanic $\delta^{7}Li$, can increase, but this shift is no longer transient and the $^{187}Os/^{188}Os$ of seawater is unaffected. Increasing and then decreasing V, to represent phases of plant colonisation and associated weathering spikes (Lenton et al., 2016), can cause a small decrease then a small increase in $^{187}Os/^{188}Os$. However, even these large and rapid changes in plant cover cannot (alone) explain the Li and Os isotope variations during Late Ordovician and Silurian events (Fig. 2). Varying D (Fig. S9) or V (Fig. S10) alters the magnitude or duration of change, but it does not affect the overall modelled trends,

which do not compare favourably to observed records. It seems more likely that a modest, slower expansion of vegetation and/or decline in degassing could have helped 'prime' the Earth system to undergo the observed events.

Enhanced weatherability of silicate rocks during the Taconic (Finlay et al., 2010) and Scandian (Munnecke et al., 2010) orogenies or the passage of volcanic rocks through the tropics during the Late Ordovician and/or Silurian (Nardin et al., 2011) could have led to significant variation in the Li and Os isotope systems. To generate the Li isotope variation seen during the Hirnantian, previous isotope modelling would require a seemingly implausible increase in uplift of ~65 % above modern levels or going from zero to roughly double the present day area of basalt (Pogge von Strandmann et al., 2017). Moreover, seawater $^{187}Os/^{188}Os$ and $\delta^{7}Li$ has been shown to be driven lower during basaltic eruptions associated with oceanic anoxic events (Lechler et al., 2015; Pogge von Strandmann et al., 2013). Therefore, plausible changes in tectonic and biological forcing, including reductions in volcanic arc degassing, expansions of terrestrial plants, orogeny or enhanced basaltic weathering fail to reconcile Os and Li isotope records or generate the required magnitude of change observed, suggesting that other causal mechanisms are required to explain isotopic variations during the Silurian.

3.4 Can orbital forcing of the organic carbon cycle explain Silurian isotope variations?

Black shale deposition in palaeotropical restricted and semi-restricted settings during the late Katian and early Rhuddanian is associated with widespread anoxia and high rates of organic carbon burial comparable to Mesozoic oceanic anoxic events (Melchin et al., 2013; Stockey et al., 2020), possibly linked to increased primary productivity from nutrients supplied by upwelling or the weathering of newly exposed glaciogenic sediments (Pohl et al., 2017). A similar pattern of black shale deposition or anoxic seafloor conditions continued until the

374 Ludlow (Page et al., 2007). Organic carbon burial on continental margins can influence
375 planetary climate and largely controls exogenic $\delta^{13}C$ values, displaying a strong correlation to
376 astronomical forcing (Kocken et al., 2019). Weaker forcing is associated with reduced
377 seasonality which drives higher annual precipitation and sediment accumulation, leading to
378 the burial of more isotopically light (^{12}C) organic carbon, and therefore higher seawater $\delta^{13}C$
379 values, and CO_2 sequestration, becoming reversed under stronger forcing (Kocken et al.,
380 2019). Additionally, lower seasonality is associated with oceanic cooling (high $\delta^{18}O$ values)
381 leading to the greater storage of organic carbon as biogenic methane ($\delta^{13}C = < -70$) in
382 submarine methane hydrates (Kocken et al., 2019). The cyclical nature of Late Ordovician to
383 Early Devonian $\delta^{13}C$ (Fig. 1J) and $\delta^{18}O$ (Fig. 1L) records has been linked to the long-term
384 ~4.5 Myr amplitude modulation of the Earth's ~400 kyr eccentricity and ~1.2 Myr obliquity
385 cycles, whereby prolonged intervals of exceptionally low forcing drove positive $\delta^{13}C$ and
386 $\delta^{18}O$ values via enhanced organic carbon burial, storage of biogenic methane and/or global
387 cooling (Sproson, 2020).

388 In order to obtain the observed > 1 ‰ variations in $\delta^{13}C$ on Myr-timescales, carbon
389 burial fluxes need to be tied to the development and decay of new carbon sinks, rather than
390 changes in carbon production and burial in existing carbon reservoirs (Laurin et al., 2015).
391 Here, we explore the potential of astronomically forced variations in marine organic carbon
392 reservoir stability as a driver of observed isotope variations. Following Laurin *et al.* (2015),
393 we assume that organic carbon moves via a series of quasi-stable reservoirs tied to the
394 efficiency of carbon burial relative to the intensity of carbon production. Below an obliquity
395 or precession threshold (th1), i.e., a period of low-amplitude insolation variation, the quasi-
396 stable reservoir of bulk organic carbon grows, sequestering atmospheric CO_2 and isotopically
397 light carbon. Between th1 and another threshold (th2), this reservoir remains stable. Above
398 th2, i.e., a period of high-amplitude insolation variation, the stored carbon is returned to the

399 exogenic reservoir as the bulk organic carbon reservoir decays, becoming a source of
400 atmospheric CO_2 and isotopically light carbon (see *Supplementary Material*). Numerical
401 astronomical models do not extend beyond 250 Ma and we therefore use sections of the
402 La2004 numerical model (Laskar et al., 2004) over the last 30 Ma (Fig. 4) as a representative
403 case for forcing Silurian palaeoclimate.

404 First, we consider obliquity forcing, using an illustrative exceptionally low obliquity
405 variation between 9.4 and 11.6 Ma (inset in Fig. 4C; Fig. 5A) to drive variations in the
406 stability of the marine sedimentary organic carbon reservoir (Fig. 5B). We assume that this
407 forcing can generate a ~5 ‰ variation in $\delta^{13}C$ (Fig. 5D), consistent with the larger Silurian
408 events recorded in the geological record (Fig. 1J), corresponding to the transient
409 accumulation of 8.5×10^4 Gt of carbon over 1.5 Myr (Fig. 5B). Such accumulation rates are
410 an order of magnitude higher than those used previously to simulate $\delta^{13}C$ variability during
411 the Cretaceous (Laurin et al., 2015). We justify this accordingly: (1) the Silurian experienced
412 a colder climate and a greater anoxic fraction of the ocean when compared to the Cretaceous
413 (Lenton et al., 2018) leading to higher levels of organic matter preservation; (2) the numerical
414 model of Laurin et al. (2015) did not account for any feedback mechanisms within the
415 carbon-cycle that would otherwise reduce the impacts of reservoir stability on planetary
416 climate; (3) we are attempting to simulate ~5 ‰ $\delta^{13}C$ variations as opposed to ~1 ‰
417 variations recorded in the Cretaceous; (4) we did not incorporate carbon storage in submarine
418 methane hydrates in our model, which would otherwise reduce accumulation rates.

419 Two maxima of organic carbon accumulation (Fig. 5B) are separated by the ~1.2 Myr
420 obliquity cycle (Fig. 5A), causing atmospheric CO_2 to decline from ~16 to ~10 PAL (Fig.
421 5C), like previous estimates for the Ordovician and Silurian (Lenton et al., 2018), before
422 obliquity forcing starts to generate net carbon release from the organic carbon reservoir (Fig.
423 5B). This corresponds to a cooling of ~2°C (Fig. 5C) and increase of ~0.5 ‰ in $\delta^{18}O_{phos}$ (Fig.

5D), smaller than variations in the conodont apatite record (Fig. 1L). The drop in atmospheric CO_2 and temperature leads to a reduction in silicate weathering, driving a decline in the ocean Os and Li reservoirs. The reduced weathering of unradiogenic silicates, such as basalt, by ~50 % relative to more radiogenic Os-rich lithologies such as sediments, leads to a ~0.1 increase in the $^{187}Os/^{188}Os$ of seawater (Fig. 5E), with peak values during minimum atmospheric pCO_2 (Fig. 5C). Meanwhile a reduction in the riverine Li flux drives a gradual increase of ~1.5 ‰ in the δ^7Li of seawater (Fig. 5E). The long ocean residence time of Li (~1.3 Myr in the model) relative to Os (~30 kyr in the model) leads to a more muted Li isotope response to climatic change when compared to Os isotopes. Although we capture the multiple peaks in Os isotopes relative to single peak in δ^7Li records, the magnitude of change is smaller and more protracted, the peaks are separated by ~1.2 Myr in the model whereas Silurian records are separated by ~0.2-0.7 Myr (Fig. 2).

Next, we consider precession forcing, using an illustrative period of exceptionally low precession variation between 9.6 to 10.6 Ma (inset in Fig. 4A; Fig. 5F) to drive variations in the stability of the marine organic carbon reservoir (Fig. 5G). This forcing can generate a similar magnitude of change to obliquity forcing (Fig. 5G-5J), but unlike obliquity forcing, the two maxima of organic carbon accumulation are separated by the ~400 kyr eccentricity cycle (Fig. 5F), leading to a transient accumulation of ~5 x 10^4 Gt of carbon over ~0.7 Myr (Fig. 5G). This places peaks in Os and Li isotopes (Fig. 5J) within the ~0.2 to 0.7 Myr range recorded in the data (Fig. 2). However, the large uncertainty associated with the age-depth model used here (Fig. 2) precludes us from discounting the influence of obliquity. Although the precession forced model improves on the obliquity model by giving a timing more consistent with the Os and Li isotope variation, the magnitude of change remains insufficient (Fig. 2). Hence, we consider an additional factor – the hypothesis that astronomical forcing of

448 the organic carbon cycle triggered intermittent glaciations during the Hirnantian and Silurian
449 (Sproson, 2020).
450
451 **3.5 Orbitally paced Silurian glaciations**
452 A decline in atmospheric CO_2 during the Late Ordovician led to extensive Southern
453 Hemisphere glaciation over Gondwana, associated with a glacio-eustatic sea-level change of
454 ~70-100 m, during the Hirnantian (Algeo et al., 2016). According to an Earth system model
455 for the Late Ordovician, there is a nonlinear response of southern hemisphere continental ice
456 sheet build-up to a decrease in radiative forcing (Pohl et al., 2016). At a pCO_2 of 16 PAL,
457 small ice caps begin to nucleate at the pole and high latitudes (≥ 60°S), but by 12 PAL ice
458 sheet feedback processes cause these sporadic glaciers to coalesce rapidly into a single
459 continental-scale ice sheet that extends to mid latitudes (45°S) where it remains relatively
460 stable. This transition corresponds to a global cooling of ~4°C and high climate sensitivity of
461 >9°C for a doubling/halving of atmospheric CO_2.
462 Running the previous obliquity (Fig. 6A) and precession forcing (Fig. 6G) of the
463 marine sedimentary organic carbon reservoir with an ice sheet and climate sensitivity derived
464 from Pohl *et al.* (2016) again leads to a transient accumulation of ~5-9 x 10^4 Gt of carbon
465 (Fig. 6B and 6H), generating a $\delta^{13}C$ variation of ~4.5-5 ‰ (Fig. 6E and 6K). With the
466 increased climate sensitivity, this drives a rapid cooling of ~4-5 °C (Fig. 6C and 6I) and an
467 increase in the Gondwanan ice sheet area of ~36 Mkm^2, expanding from ~90°S to ~45°S,
468 equating to a glacioeustatic drop of ~65 m (Fig. 6D and 6J). Subsequent net carbon loss can
469 generate a recovery of CO_2 to ~15 PAL, warming of ~4 °C, and shrinkage of ice sheets to ~5-
470 10 Mkm^3. Then, a further phase of net carbon accumulation causes CO_2 to decline to ~11
471 PAL, corresponding cooling of ~4 °C (Fig. 6C and 6I), and ice sheets again expanding to 36

472 Mkm^3 (Fig. 6D and 6J). Then, as eccentricity or obliquity variation increases again, net
473 carbon loss causes CO_2 to rise to ~18 PAL, eliminating ice sheets.
474 Projected cooling is comparable to estimated temperature anomalies of >5°C for the
475 Ludlow and Přídolí (Trotter et al., 2016) whilst modelled sea-level change is comparable to
476 reconstructed sea-level variations of 50-80 m during Silurian climate events (Fig. 1M).
477 Cooling coupled to an increase in ice volume, which directly influences the $\delta^{18}O$ of seawater,
478 leads to a $\delta^{18}O_{phos}$ increase of ~2 ‰ (Fig. 6E and 6K), similar to $\delta^{18}O$ perturbations recorded
479 in the Silurian conodont apatite record (Fig. 1L). Following a series of sensitivity tests, a
480 doubling of the average thickness of the ice sheet from 1 km to 2 km (Fig. 7A) increases the
481 magnitude of $\delta^{18}O_{phos}$ variability from ~2 ‰ to ~2.5 ‰ (Fig. 7C). Tripling the thickness of
482 the ice sheet to 3 km (Fig. 7D), consistent with Pohl et al.'s (2016) simulations, increases the
483 magnitude of $\delta^{18}O_{phos}$ variability to ~3.5 ‰ (Fig. 7F), consistent with conodont apatite
484 records for the Hirnantian (Trotter et al., 2008) and Mid-Ludfordian (Frýda et al., 2021), but
485 generally higher than other Silurian records (Trotter et al., 2016). An increase in ice thickness
486 to 2 and 3 km drives a larger sea-level drop of 120 m and 190 m, respectively (Fig. 7B and
487 7E). The former is comparable to sea-level estimates for the Hirnantian whilst the latter is far
488 higher than anything interpreted for the Ordovician and Silurian (Haq and Schutter, 2008).
489 This suggests that although the Hirnantian glaciation likely had an ice sheet thickness of up to
490 ~3 km, Silurian ice sheets were much smaller, reaching an average ice sheet thickness closer
491 to ~1 km, explaining the lack of marine terminating glaciers and the therefore glacial tillites
492 in the post-Sheinwoodian geological record (Fig. 1K) and low amplitude sea level variation
493 (Calner, 2008).
494 A reduced riverine flux of Os and Li, coupled to a shift to more incongruent
495 weathering due to increased clay formation caused by a longer continental residence time of
496 water, proposed for the Hirnantian glaciation (Pogge von Strandmann et al., 2017), causes an

497 increase in the $^{187}Os/^{188}Os$ of seawater and the δ^7Li of carbonate by ~0.13-0.2 and ~2.5-4.5
498 ‰, respectively (Fig. 6F and 6L), still substantially lower than recorded values (Fig. 2).
499 Although it is not possible to estimate the exact parameters governing the isotope systems
500 during the Palaeozoic, we speculate as to the possible causes of discrepancies between
501 modelled and observed data based on known processes. Physical erosion of Os-rich
502 sediments, such as shales and pyrite, in response to the expansion of large scale rock-grinding
503 glaciers has been shown to influence the Late Pleistocene Os record through the injection of
504 radiogenic Os to the ocean (Georg et al., 2013). Doubling sediment weathering (Fig. 7H)
505 with maximum ice sheet extent (Fig. 7G), to mimic the erosion of Os-rich lithologies,
506 increases the magnitude of the $^{187}Os/^{188}Os$ response to ~0.4 (Fig. 7I) on a similar order to
507 Silurian records (Fig. 2). The residence time of Li in the ocean is estimated to be ~1 to 1.5
508 Myr for the present day (Huh et al., 1998), but if we assume that the oceanic Li residence
509 time was half that of the present, due to a higher Li removal rate on continental margins with
510 a higher sediment accumulation rate than present (Fig. 7K), the δ^7Li of seawater increases by
511 ~4-5 ‰ (Fig. 7L). Additionally, if we assume that the δ^7Li of riverine inputs underwent a
512 larger fractionation of 20 ‰, due to even higher clay formation associated with the expansion
513 of ice sheets (Fig. 7M-N), the magnitude of the seawater δ^7Li response increases to ~7-10 ‰
514 (Fig. 7O).

515 Finally, numerical models used here generate multiple peaks in $\delta^{13}C$ tied to
516 eccentricity or obliquity minima (Fig. 6E, K) which are not clearly observed in $\delta^{13}C$ records
517 (Fig. 1J). This discrepancy could be an artefact of undersampling incomplete geological
518 sections, indicating the need for more complete Silurian $\delta^{13}C$ records. For example,
519 exceptionally complete sedimentary records for the Hirnantian reveal several $\delta^{13}C$ cycles
520 associated with glacial apices, similar to our model, that would otherwise be missing due to
521 hiatuses during sea level lowstands (Ghienne et al., 2014). Alternatively, simply forcing

organic carbon burial alone may be too simplistic to recreate the full complexity of records, and an interactive organic carbon cycle and/or additional forcing mechanisms, such as volcanic arc degassing or land-plant development, may be needed to reconcile numerical models with the geological record.

4. Conclusion

The $^{187}Os/^{188}Os$, $\delta^{7}Li$, $\delta^{13}C$, $\delta^{18}O$, and sea level response from our dynamic carbon-osmium-lithium-model can recreate the variability within Os and Li isotope records from this study and the magnitude of $\delta^{13}C$, $\delta^{18}O$ and sea-level records from the literature, combining all lines of evidence under one causal mechanism for the first time. We propose that the long-term ~4.5 Myr amplitude modulation of the Earth's orbital eccentricity and/or obliquity led to prolonged periods of high organic carbon burial, atmospheric CO_2 drawdown, cooling and continental glaciation during the Hirnantian, the early Sheinwoodian, the Homerian, the mid Ludfordian and the late Přídolí-early Lochkovian, extending the notion of 'Cenozoic-style' glacial cycles and high-order phenomena during the Late Ordovician (Ghienne et al., 2014) to the Silurian. Dramatic cooling or eustatic regression associated with glaciations and/or preceding marine anoxic/euxinic conditions would have removed the habitat space of marine taxa leading to extinctions including the Late Ordovician, 'Ireviken', 'Mulde', 'Lau' and 'Silurian-Devonian Boundary' events.

Due to the large uncertainty associated with the age model used in this study, and potential temporal aliasing arising from the under-sampling of incomplete geological sections, we are unable to determine whether eccentricity or obliquity was the dominant pace setter for Silurian glaciations. Future work should look to develop high resolution records with improved age control, akin to Ghienne et al. (2014), for the Silurian. Finally, the dynamic model developed in this study is too simplistic (see section 4.8 in the *Supplementary*

547 *Material*) to recreate the nuances of observed Hirnantian and Silurian records. More complex
548 modelling that includes a full description of the Earth's C-O-N-P-S cycles (e.g., Lenton et al.,
549 2018) and ice-sheet feedbacks (e.g., Pohl et al., 2016) is needed to fully reconcile the forcing
550 parameters explored here with Silurian records.
551
552 **Acknowledgements**
553 A.D. Sproson would like to thank the Geological Society of London's William George
554 Fearnsides fund and the College of St. Hild and St. Bede's (Durham University) John
555 Simpson Greenwell Memorial Fund for partially funding this research. P. A. E. Pogge von
556 Strandmann acknowledges financial support from the ERC grant 682760
557 CONTROLPASTCO2. D. Selby acknowledges support from the TOTAL Endowment Fund
558 and the Dida Scholarship of CUG Wuhan. J. Frýda was supported by GAGR (grant No. 17-
559 18120S). T.M. Lenton was supported by NERC (NE/N018508/1, NE/P013651/1). L. Slavík
560 was supported by GACR (grant No. GA17-06700S) and together with J. Hladil received
561 institutional support from RVO 67985831. Finally, we would like to thank T. Lyons and
562 three anonymous reviewers for their constructive comments which greatly improved this
563 manuscript.
564
565 **Appendix A. Supplementary material**
566 The supplementary material contains a description of the geological setting, supplementary
567 results, age-depth model, and the dynamic C-Os-Li geochemical model along with Table S1-
568 S3 and Fig. S1-S10. An excel version of the supplementary tables, including Re-Os data for
569 the USGS rock reference material SBC-1 (Table S4), and dynamic C-Os-Li geochemical
570 models used in this study are also provided.

571 **Figures**

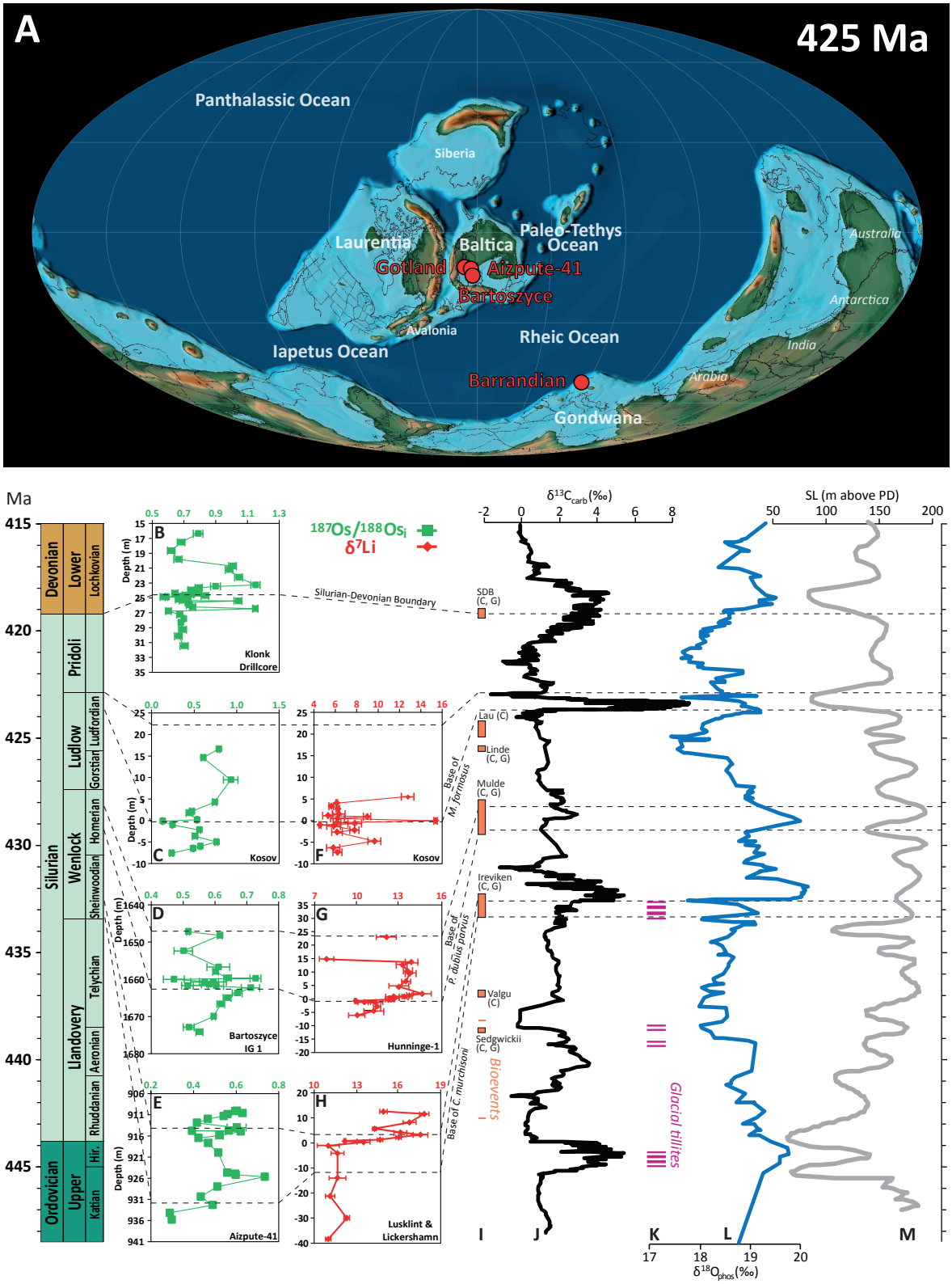

572 **Fig. 1.** Palaeoclimate records for the Upper Ordovician to the Lower Devonian. (**A**)

573 Palaeogeographic reconstruction of the Wenlock (425 Ma) with sample locations highlighted

574 by red circles (Scotese, 2016). Osmium (green squares) and δ^7Li (red diamonds) isotope data

575 are shown for the Klonk (**B**), Kosov (**C** and **F**), Bartoszyce IG-1 (**D**), Aizpute-41 (**E**),
576 Hunninge-1 (**G**), Lusklint (**H**) and Lickershamn (**H**) sections (see Fig. S1-S7 for more
577 details). Regional data sets from this study are compared to global conodont (C) and
578 graptolite (G) bioevents (**I**), carbonate $\delta^{13}C$ (**J**), glacial tillites (**K**) conodont apatite $\delta^{18}O$ (**L**)
579 and eustatic SL (**M**) records (Caputo et al., 1998; Díaz-Martínez and Grahn, 2007; Grahn and
580 Caputo, 1992; Haq and Schutter, 2008; Sproson, 2020; Trotter et al., 2008; Trotter et al.,
581 2016).
582

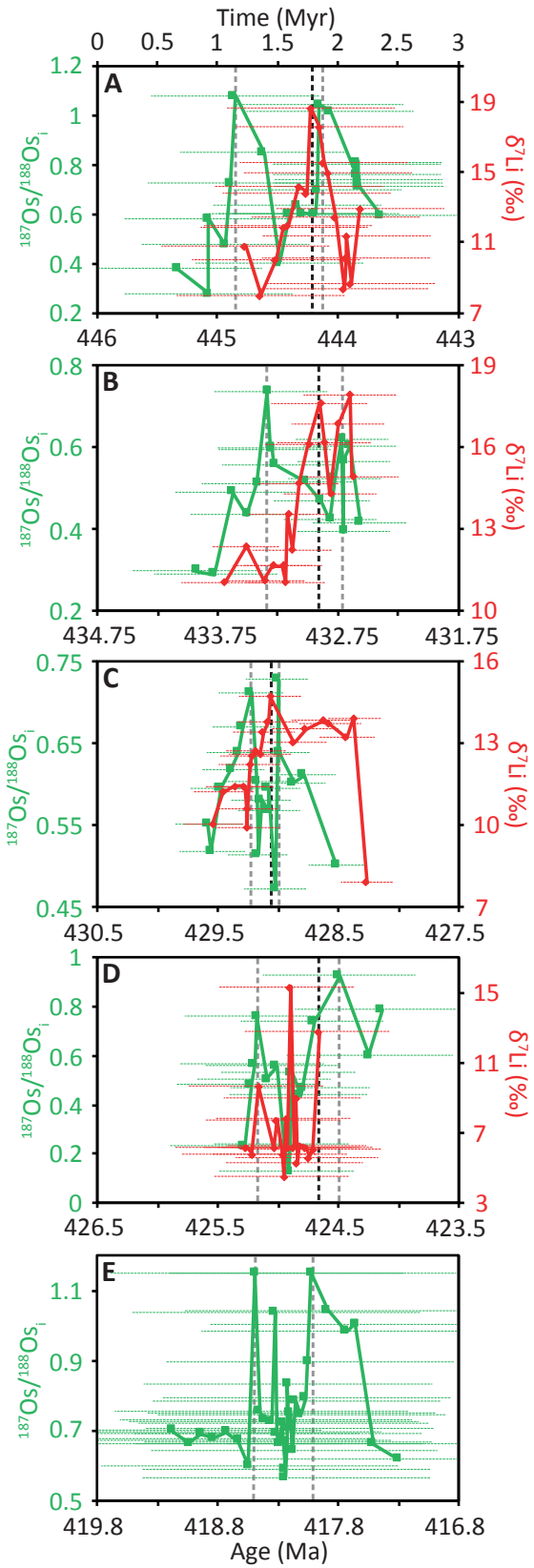

583 **Fig. 2.** Osmium and lithium isotope data for the Hirnantian (Finlay et al., 2010; Pogge von
584 Strandmann et al., 2017) (**A**), Telychian-Sheinwoodian boundary (**B**), mid-Homerian (**C**),
585 mid-Ludfordian (**D**) and Přídolí-Lochkovian boundary (**E**) compiled onto our new age-depth

model (Fig. S8). The vertical dashed grey and black lines highlight the key respective features of Os and Li isotope variation the dynamic carbon-osmium-lithium-model will attempt to recreate. The horizontal dashed lines represent 1σ age uncertainty for Os (green) and Li (red) isotope records.

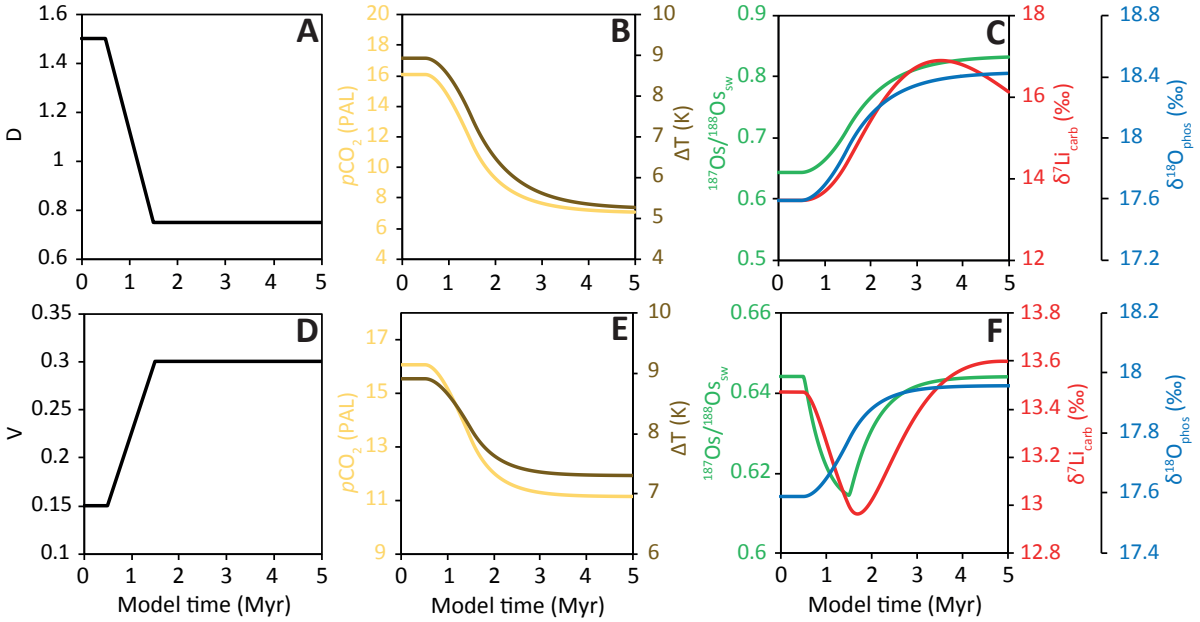

591 **Fig. 3.** The effect of degassing (A-C) and vegetation (D-F) on the O, Os and Li isotope systems

592 using a dynamic carbon-osmium-lithium-model.

593

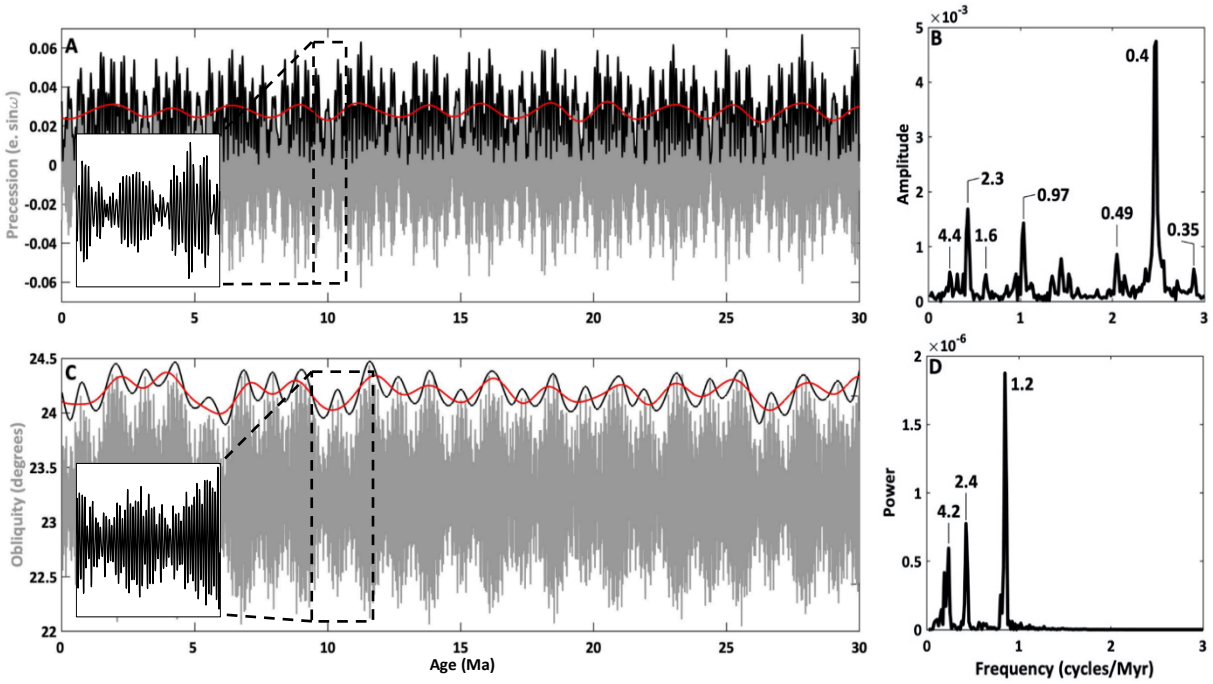

Fig. 4. Orbital records for the last 30 Myr**.** Precession (**A**) and obliquity (**C**) from the La2004 numerical model (grey) (Laskar et al., 2004) used to drive carbon-cycle models (inset of **A** and **B**). The eccentricity (**A**) and the amplitude modulation of obliquity (**C**) along with their ~2.4 Myr (0 to 0.7 cycles/myr) low pass filtering are show by black and red lines, respectively. A periodogram of the eccentricity (**B**) and the obliquity amplitude modulation (**D**) are shown along with dominant periods (Myr) (Sproson, 2020).

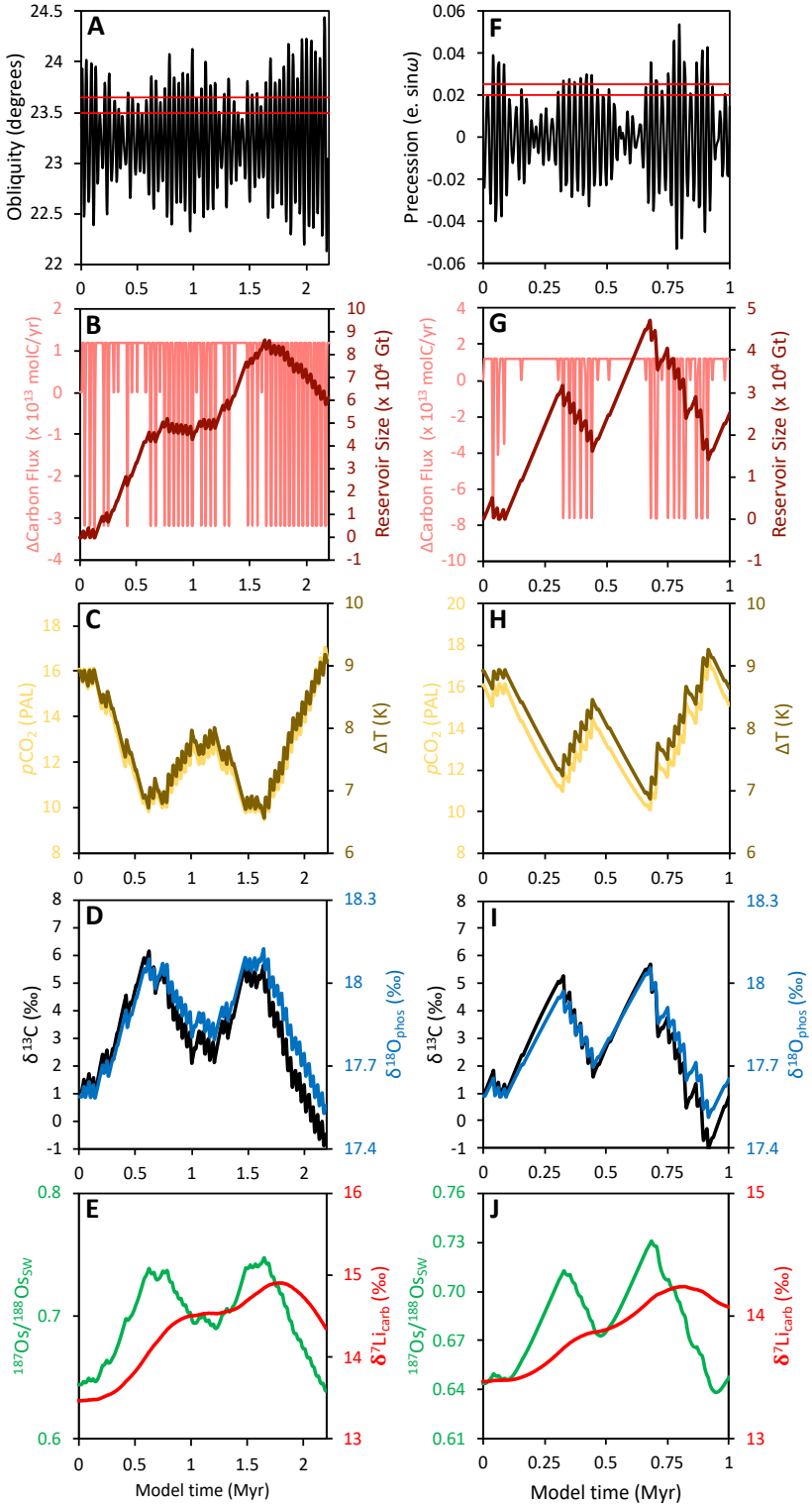

Fig. 5. The effect of an astronomically controlled quasi-stable reservoir on the C, O, Os and Li isotope systems. Modelled for a period of exceptionally low obliquity (**A**-**E**) and precession (**F**-**J**) variability using a dynamic carbon-osmium-lithium-model.

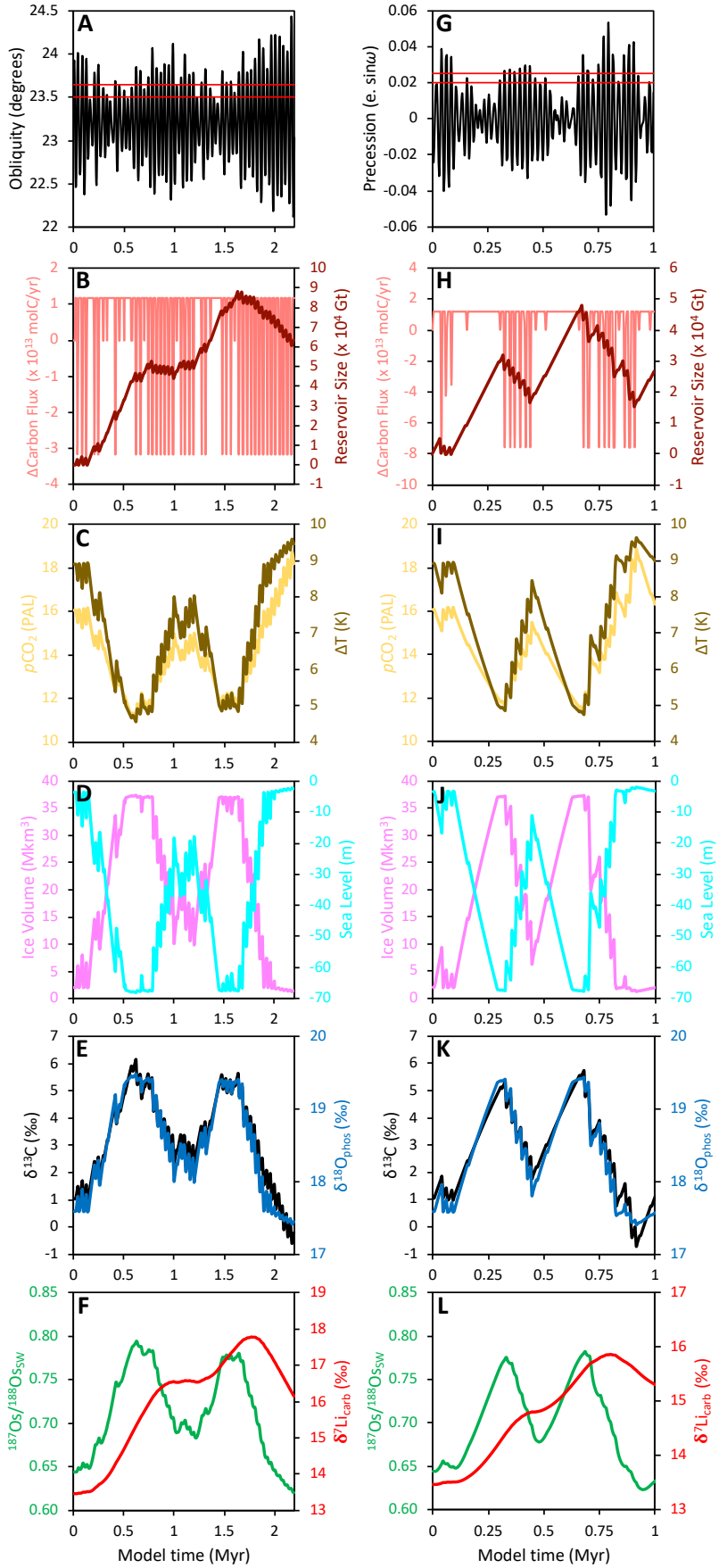

606 **Figure 6.** The effect of an astronomically controlled quasi-stable reservoir on the C, O, Os

607 and Li isotope systems for a period of exceptionally low obliquity (**A**-**F**) and precession (**G**-
608 **L**) variability. As opposed to scenarios presented in Fig. 3 and Fig. 5, the ice sheet and
609 climate sensitivity of Pohl *et al.* (2016) has been added.
610

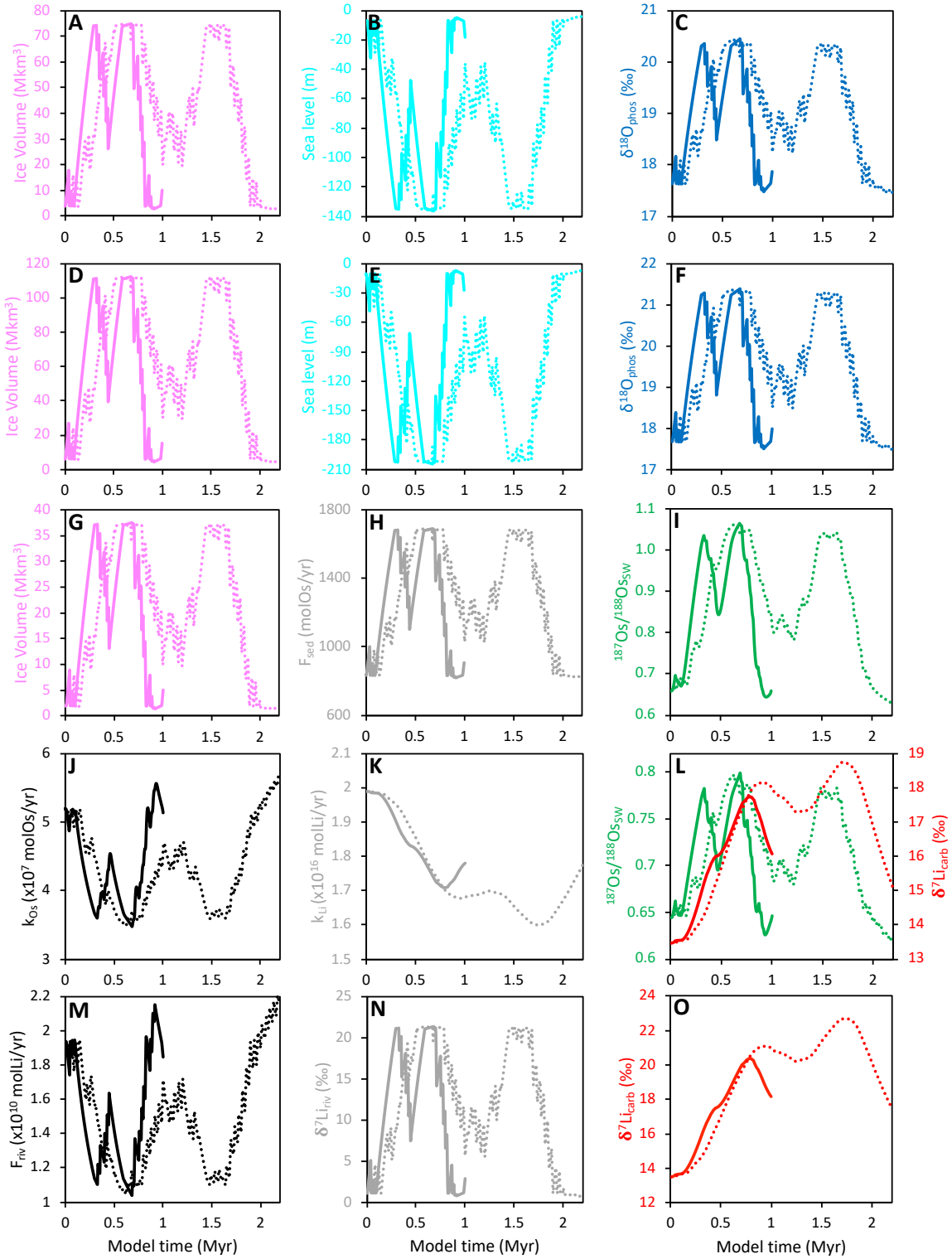

Fig. 7. Sensitivity studies for the effect of an astronomically controlled quasi-stable reservoir on the C, O, Os and Li isotope systems for a period of exceptionally low obliquity (dashed lines) and precession (solid lines) variability with the ice sheet and climate sensitivity of Pohl *et al.* (Pohl et al., 2016). Sensitivity studies are as follows: ice volume, sea level and $\delta^{18}O_{phos}$

for an ice sheet thickness of 2 km (**A-C**) and 3 km (**D-F**); the effect of tying ice volume (**G**) to sedimentary Os flux (**H**) on the $^{187}Os/^{188}Os$ of seawater (**I**) after replacing Eq. 29 with Eq. 31; the influence of doubling the partition coefficient (k) of Os (**J**) and Li (**K**) on the $^{187}Os/^{188}Os_{sw}$ and δ^7Li_{carb} values (**L**); the effect of increasing the fractionation factor of the Li riverine endmember to 20 ‰ (**M** and **N**) on δ^7Li_{carb} (**O**).

References

Algeo, T.J., Marenco, P.J., Saltzman, M.R., 2016. Co-evolution of oceans, climate, and the biosphere during the 'Ordovician Revolution': A review. Palaeogeography, Palaeoclimatology, Palaeoecology 458, 1-11.

Berner, R.A., 2006. GEOCARBSULF: A combined model for Phanerozoic atmospheric O2 and CO2. Geochimica et Cosmochimica Acta 70, 5653-5664.

Bickert, T., Pätzold, J., Samtleben, C., Munnecke, A., 1997. Paleoenvironmental changes in the Silurian indicated by stable isotopes in brachiopod shells from Gotland, Sweden. Geochimica et Cosmochimica Acta 61, 2717-2730.

Calner, M., 2008. Silurian global events – at the tipping point of climate change, in: Elewa, A.M.T. (Ed.), Mass Extinction. Springer Berlin Heidelberg, Berlin, Heidelberg, pp. 21-57.

Caputo, M.V., Landing, E., Johnson, M., 1998. Ordovician–Silurian glaciations and global sea-level changes. Silurian cycles, 15-25.

Crampton, J.S., Meyers, S.R., Cooper, R.A., Sadler, P.M., Foote, M., Harte, D., 2018. Pacing of Paleozoic macroevolutionary rates by Milankovitch grand cycles. Proceedings of the National Academy of Sciences 115, 5686-5691.

Creaser, R., Papanastassiou, D., Wasserburg, G., 1991. Negative thermal ion mass spectrometry of osmium, rhenium and iridium. Geochimica et Cosmochimica Acta 55, 397-401.

Cumming, V.M., Poulton, S.W., Rooney, A.D., Selby, D., 2013. Anoxia in the terrestrial environment during the late Mesoproterozoic. Geology 41, 583-586.

Díaz-Martínez, E., Grahn, Y., 2007. Early Silurian glaciation along the western margin of Gondwana (Peru, Bolivia and northern Argentina): Palaeogeographic and geodynamic setting. Palaeogeography, Palaeoclimatology, Palaeoecology 245, 62-81.

Finlay, A.J., Selby, D., Gröcke, D.R., 2010. Tracking the Hirnantian glaciation using Os isotopes. Earth and Planetary Science Letters 293, 339-348.

Flesch, G.D., Anderson, A.R., Svec, H.J., 1973. A secondary isotopic standard for 6Li/7Li determinations. International Journal of Mass Spectrometry and Ion Physics 12, 265-272.

Frýda, J., Lehnert, O., Joachimski, M.M., Männik, P., Kubajko, M., Mergl, M., Farkaš, J., Frýdová, B., 2021. The Mid-Ludfordian (late Silurian) Glaciation: A link with global changes in ocean chemistry and ecosystem overturns. Earth-Science Reviews 220, 103652.

Georg, R.B., West, A.J., Vance, D., Newman, K., Halliday, A.N., 2013. Is the marine osmium isotope record a probe for CO2 release from sedimentary rocks? Earth and Planetary Science Letters 367, 28-38.

Ghienne, J.-F., Desrochers, A., Vandenbroucke, T.R.A., Achab, A., Asselin, E., Dabard, M.-P., Farley, C., Loi, A., Paris, F., Wickson, S., Veizer, J., 2014. A Cenozoic-style scenario for the end-Ordovician glaciation. Nature Communications 5, 4485.

Grahn, Y., Caputo, M.V., 1992. Early Silurian glaciations in Brazil. Palaeogeography, Palaeoclimatology, Palaeoecology 99, 9-15.
Haq, B.U., Schutter, S.R., 2008. A Chronology of Paleozoic Sea-Level Changes. Science 322, 64-68.
Huh, Y., Chan, L.-H., Zhang, L., Edmond, J.M., 1998. Lithium and its isotopes in major world rivers: implications for weathering and the oceanic budget. Geochimica et Cosmochimica Acta 62, 2039-2051.
Jeppsson, L., 1990. An oceanic model for lithological and faunal changes tested on the Silurian record. Journal of the Geological Society 147, 663-674.
Kocken, I.J., Cramwinckel, M.J., Zeebe, R.E., Middelburg, J.J., Sluijs, A., 2019. The 405 kyr and 2.4 Myr eccentricity components in Cenozoic carbon isotope records. Clim. Past 15, 91-104.
Laskar, J., Robutel, P., Joutel, F., Gastineau, M., Correia, A.C.M., Levrard, B., 2004. A long-term numerical solution for the insolation quantities of the Earth. A&A 428, 261-285.
Laurin, J., Meyers, S.R., Uličný, D., Jarvis, I., Sageman, B.B., 2015. Axial obliquity control on the greenhouse carbon budget through middle- to high-latitude reservoirs. Paleoceanography 30, 133-149.
Lechler, M., Pogge von Strandmann, P.A.E., Jenkyns, H.C., Prosser, G., Parente, M., 2015. Lithium-isotope evidence for enhanced silicate weathering during OAE 1a (Early Aptian Selli event). Earth and Planetary Science Letters 432, 210-222.
Lenton, T.M., Crouch, M., Johnson, M., Pires, N., Dolan, L., 2012. First plants cooled the Ordovician. Nature Geoscience 5, 86-89.
Lenton, T.M., Dahl, T.W., Daines, S.J., Mills, B.J.W., Ozaki, K., Saltzman, M.R., Porada, P., 2016. Earliest land plants created modern levels of atmospheric oxygen. Proceedings of the National Academy of Sciences 113, 9704-9709.
Lenton, T.M., Daines, S.J., Mills, B.J.W., 2018. COPSE reloaded: An improved model of biogeochemical cycling over Phanerozoic time. Earth-Science Reviews 178, 1-28.
Loydell, D.K., Frýda, J., 2011. At what stratigraphical level is the mid Ludfordian (Ludlow, Silurian) positive carbon isotope excursion in the type Ludlow area, Shropshire, England. Bulletin of Geosciences 86, 197-208.
McKenzie, N.R., Horton, B.K., Loomis, S.E., Stockli, D.F., Planavsky, N.J., Lee, C.-T.A., 2016. Continental arc volcanism as the principal driver of icehouse-greenhouse variability. Science 352, 444-447.
Melchin, M.J., Mitchell, C.E., Holmden, C., Štorch, P., 2013. Environmental changes in the Late Ordovician–early Silurian: Review and new insights from black shales and nitrogen isotopes. GSA Bulletin 125, 1635-1670.
Misra, S., Froelich, P.N., 2012. Lithium Isotope History of Cenozoic Seawater: Changes in Silicate Weathering and Reverse Weathering. Science 335, 818.
Munnecke, A., Calner, M., Harper, D.A.T., Servais, T., 2010. Ordovician and Silurian sea–water chemistry, sea level, and climate: A synopsis. Palaeogeography, Palaeoclimatology, Palaeoecology 296, 389-413.
Munnecke, A., Samtleben, C., Bickert, T., 2003. The Ireviken Event in the lower Silurian of Gotland, Sweden – relation to similar Palaeozoic and Proterozoic events. Palaeogeography, Palaeoclimatology, Palaeoecology 195, 99-124.
Nardin, E., Goddéris, Y., Donnadieu, Y., Hir, G.L., Blakey, R.C., Pucéat, E., Aretz, M., 2011. Modeling the early Paleozoic long-term climatic trend. GSA Bulletin 123, 1181-1192.
Nowell, G., Luguet, A., Pearson, D., Horstwood, M., 2008. Precise and accurate 186 Os/188 Os and 187 Os/188 Os measurements by multi-collector plasma ionisation mass spectrometry (MC-ICP-MS) part I: Solution analyses. Chemical Geology 248, 363-393.

Page, A., Zalasiewicz, J., Williams, M., Popov, L., 2007. Were transgressive black shales a negative feedback modulating glacioeustasy in the Early Palaeozoic Icehouse. Page 123-156 . Special Publication of the Geological Society of London, The Micropalaeontological Society.
Peucker-Ehrenbrink, B., Ravizza, G., 2000. The marine osmium isotope record. Terra Nova 12, 205-219.
Pogge von Strandmann, P.A., Desrochers, A., Murphy, M., Finlay, A., Selby, D., Lenton, T., 2017. Global climate stabilisation by chemical weathering during the Hirnantian glaciation. Geochemical Perspectives Letters 3, 230-237.
Pogge von Strandmann, P.A.E., Jenkyns, H.C., Woodfine, R.G., 2013. Lithium isotope evidence for enhanced weathering during Oceanic Anoxic Event 2. Nature Geoscience 6, 668-672.
Pogge von Strandmann, P.A.E., Schmidt, D.N., Planavsky, N.J., Wei, G., Todd, C.L., Baumann, K.-H., 2019. Assessing bulk carbonates as archives for seawater Li isotope ratios. Chemical Geology 530, 119338.
Pohl, A., Donnadieu, Y., Le Hir, G., Ferreira, D., 2017. The climatic significance of Late Ordovician‐early Silurian black shales. Paleoceanography 32, 397-423.
Pohl, A., Donnadieu, Y., Le Hir, G., Ladant, J.-B., Dumas, C., Alvarez-Solas, J., Vandenbroucke, T.R.A., 2016. Glacial onset predated Late Ordovician climate cooling. Paleoceanography 31, 800-821.
Rasmussen, C.M.Ø., Kröger, B., Nielsen, M.L., Colmenar, J., 2019. Cascading trend of Early Paleozoic marine radiations paused by Late Ordovician extinctions. Proceedings of the National Academy of Sciences 116, 7207.
Sauzéat, L., Rudnick, R.L., Chauvel, C., Garçon, M., Tang, M., 2015. New perspectives on the Li isotopic composition of the upper continental crust and its weathering signature. Earth and Planetary Science Letters 428, 181-192.
Scotese, C., 2016. PALEOMAP PaleoAtlas for GPlates and the PaleoData Plotter Program, PALEOMAP Project. See http://www.earthbyte.org/paleomap-paleoatlas-for-gplates (accessed 1st October 2019).
Selby, D., Creaser, R.A., 2003. Re–Os geochronology of organic rich sediments: an evaluation of organic matter analysis methods. Chemical Geology 200, 225-240.
Smoliar, M.I., Walker, R.J., Morgan, J.W., 1996. Re-Os Ages of Group IIA, IIIA, IVA, and IVB Iron Meteorites. Science 271, 1099-1102.
Sproson, A.D., 2020. Pacing of the latest Ordovician and Silurian carbon cycle by a ~4.5 Myr orbital cycle. Palaeogeography, Palaeoclimatology, Palaeoecology 540, 109543.
Stockey, R.G., Cole, D.B., Planavsky, N.J., Loydell, D.K., Frýda, J., Sperling, E.A., 2020. Persistent global marine euxinia in the early Silurian. Nature Communications 11, 1804.
Sutcliffe, O.E., Dowdeswell, J.A., Whittington, R.J., Theron, J.N., Craig, J., 2000. Calibrating the Late Ordovician glaciation and mass extinction by the eccentricity cycles of Earth's orbit. Geology 28, 967-970.
Trotter, J.A., Williams, I.S., Barnes, C.R., Lécuyer, C., Nicoll, R.S., 2008. Did Cooling Oceans Trigger Ordovician Biodiversification? Evidence from Conodont Thermometry. Science 321, 550-554.
Trotter, J.A., Williams, I.S., Barnes, C.R., Männik, P., Simpson, A., 2016. New conodont δ18O records of Silurian climate change: Implications for environmental and biological events. Palaeogeography, Palaeoclimatology, Palaeoecology 443, 34-48.